RESEARCH ARTICLE | JULY 14 2022

Ion shock layer formation during multi-ion-species plasma jet stagnation events [REE]

A. I. Mohammed (i); C. S. Adams (ii)



Phys. Plasmas 29, 072307 (2022) https://doi.org/10.1063/5.0087509

A CHORUS





CrossMark





Ion shock layer formation during multi-ion-species plasma jet stagnation events

Cite as: Phys. Plasmas 29, 072307 (2022); doi: 10.1063/5.0087509

Submitted: 6 February 2022 · Accepted: 16 June 2022 ·

Published Online: 14 July 2022







A. I. Mohammed 🕞 and C. S. Adams^{a)} 🝺

AFFILIATIONS

Virginia Polytechnic Institute and State University, Center for Space Science and Engineering Research, Blacksburg, Virginia 24061, USA

a) Author to whom correspondence should be addressed: csadams@vt.edu

ABSTRACT

We report the characteristics of collisional plasma shocks formed during interactions between low density ($n_e \approx 10^{15}$ cm⁻³), low temperature ($T_e \approx 2$ eV), high velocity (30 km s⁻¹), plasma jets and stagnant plasma of similar parameters. This investigation seeks to probe the structure of shocks in multi-ion-species plasmas, in particular, the presence of gradient-driven ion species separation at the shock front. The railgun-accelerated jets utilized here have previously been shown to exist in a collisional regime with intra-jet collisional mean-free-path substantially smaller than jet size [Schneider *et al.*, Plasma Sources Sci. Technol. **29**, 045013 (2020)]. To induce collisions, a dielectric barrier is located downstream of the railgun to stagnate an initially supersonic plasma jet. Around the time of stagnation, the railgun emits a second jet which shortly collides with the stagnant plasma. The presence of a structure emitting in the UV-visible band is evident in high-speed photographs of the moments immediately following the arrival of the second jet at the stagnant plasma. Analysis of interferometric and spectroscopic data suggests that the observed increase in density from the jet to the post-collision plasma is consistent with the formation of a bow shock structure with a multi-millimeter-scale ion shock layer.

Published under an exclusive license by AIP Publishing. https://doi.org/10.1063/5.0087509

I. INTRODUCTION

Interactions between colliding low density, high Mach number plasma jets as well as those between jets and stationary background plasmas provide a readily diagnosable laboratory configuration to study shocks and diffusive phenomena in collisional and marginally collisional plasmas.^{2–4} Described here are the observations of shocks layers recorded within a broader campaign to characterize the distribution of ions within the electron preheat layer of hydrodynamic shocks formed in such experiments. The preheat layer is of particular interest since differential gradient-driven ion diffusion is widely predicted to cause species separation in this region,⁵⁻⁷ but direct evidence of this process has only recently been observed in experiments, complementing previous measurements consistent with the presence of such separation in laser-driven experiments9 and in inertial-confinement-fusion (ICF) implosions. 10-12 Computational and theoretical studies of shocks expected to be present in ICF experiments have suggested that the propagation of shock waves through fusion fuel could lead to a separation of ion species across the shock front, potentially degrading fusion yield. 13-18 It has also been suggested that shock waves may play a role in the evolution of the fusion burn and features in the observed light curve^{20,21} of Type-II supernovae. However,

outstanding questions remain with regard to the underlying shock physics in all of these scenarios, specifically the role of non-local-thermodynamic-equilibrium (LTE) effects and changing ionization states in the region of the shock. The results reported here contribute to the growing database of experimental shock studies that provide insights into these questions and will be available to benchmark physics models relevant to both space and fusion plasmas.

In the experiments reported here, a series of plasma jets are formed and accelerated by a linear plasma armature railgun during each experimental pulse. While previous efforts¹ involved characterizing unobstructed jets, in these experiments a solid dielectric (polycarbonate) target obstructs the jet flight path in order to induce jet stagnation. In this new configuration, we characterize the collisions that occur between plasma from the stagnated first jet and a supersonic second jet. Since the mean ionization state $\bar{Z} \geq 1$ for the stagnant plasma and the jet, we consider the interaction to be dominated by Coulomb collisions between charged particles. Noninvasive spectroscopic and interferometric diagnostics record the interaction, enabling assessment of the properties of the shocks present and the potential for these experiments to produce observable species separation in plasma shocks.

We first describe the experimental setup and diagnostics used in this study (Sec. II) before qualitatively and quantitatively discussing the evolution of the collision event for two obstruction positions (Secs. III–VI). We then analyze spectroscopic and interferometric measurements with the aid of non-LTE collisional-radiative modeling to characterize the gradients in ion and electron density that occur during collision events (Secs. VII and VIII). Finally, we discuss the suitability of the present experimental configuration to characterize plasma shocks based on the evaluation of parameters relevant to jet collisionality.

II. EXPERIMENTAL APPARATUS

A single argon-fed linear armature plasma railgun¹ serves as the plasma source in this study. In addition to argon, the jets produced by the railgun also consist of impurity species that are ablated from the plasma-facing components of the gun during discharge. Based on the chemical composition of the railgun components and capacitance manometer measurements of the post-shot pressure rise for gasinjection only and energized discharges, we estimate the jet composition to be $86 \pm 14\%$ argon, with the remaining material assumed to consist of carbon, nitrogen, hydrogen, boron, aluminum, and oxygen.

As described in previous work, the railgun is mounted on a $0.76\,\mathrm{m}^3$, $1.2\,\mathrm{m}$ long cylindrical vacuum chamber such that the gun's bore-sight axis is collinear with the z-axis of the chamber. All z-axis measurements are referenced to the muzzle of the railgun. Multiple jets are accelerated during each experimental pulse due to the underdamped current waveform that energizes the railgun. To induce jet collisions within a single discharge cycle, a $40 \times 40\,\mathrm{cm}^2$, 6 mm thick polycarbonate sheet has been installed in the chamber at positions either 12 or 17 cm away from the muzzle of the railgun. Upon reaching this obstruction, the first jet stagnates, resulting in a background plasma with which subsequent jets in the discharge cycle collide. The results presented in this paper detail the interaction between the second jet and stagnated first jet for obstruction locations of $z_{pc} = 12$ and 17 cm.

The primary diagnostics used in these experiments include a two-chord heterodyne Mach–Zehnder interferometer, an image intensified CCD camera, and a high wavelength resolution spectrometer equipped with imaging optics. Interferometer probe beams were arranged in a single-pass configuration along the chords perpendicular to the bore-sight axis. Every few shots, the positions of the probe beams were changed to characterize electron density at various axial and radial locations relative to the bore-sight axis.

A Princeton Instruments PI-MAX4 1024i (1024 \times 1024 pixel) image-intensified CCD camera recorded the collision events in the UV-visible spectrum for both obstruction locations. Equipped with a 25 mm focal length lens, f/8 aperture, and exposure times as short as 3 ns, the camera was positioned atop the vacuum chamber such that its viewing chord intersects the bore-sight axis at 90°.

For shots where fast photography was not employed, the same imaging unit served as the detector for a Princeton Instruments SP-2758 series spectrograph. The spectrometer has a 750 m focal length and utilized a survey wavelength range of 430 to 490 nm. Gate times of 200 ns were utilized in these experiments to temporally resolve plasma emission. Spectrometer collection optics, shown in Fig. 1, were also placed atop the vacuum chamber at a 90° angle to the bore-sight axis.

An optical system was designed for the spectrometer that projects UV-visible radiation emitted by the plasma onto a linear array of

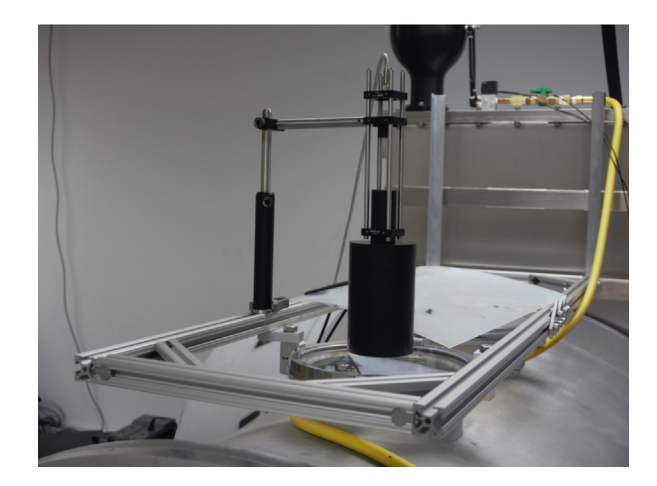


FIG. 1. Spectrometer collection optics with fiber bundle (in stainless steel sheath) entering the telescope from top.

seven, 200 μm core diameter multimode fibers, resulting in spatially resolved spectrograms. Table I provides the fiber viewing chords for each experimental configuration. The fiber bundle couples to the entrance slit of the spectrometer, which was kept at a width of 10 μm . The design of this fiber-coupled optical system and the intensifier gate time on the CCD detector allows for the collection of spectral data

TABLE I. Spectrometer viewing chord dimensions for each fiber along the bore-sight axis for each experimental configuration. All measurements are referenced to the muzzle of the railgun.

Experimental config. (cm)	Fiber number	Chord view range (cm)
$z_{\rm pc} = 12$ (imaging collision event)	A1	11.49-11.71
	A2	11.15-11.37
	A3	10.81-11.03
	A4	10.47-10.69
	A5	10.13-10.35
	A6	9.80-10.01
	A7	9.46-9.68
$z_{\rm pc} = 17$ (imaging collision event)	B1	16.28-16.52
	B2	15.93-16.16
	В3	15.57-15.80
	B4	15.22-15.45
	B5	14.86-15.09
	В6	14.51-14.74
	B7	14.15-14.38
$z_{\rm pc} = 17$ (imaging unobstructed jets)	C1	11.79-11.99
	C2	11.50-11.70
	C3	11.21-11.41
	C4	10.93-11.13
	C5	10.64-10.84
	C6	10.35-10.55
	C7	10.07-10.27

with \sim 200 ns scale temporal resolution and millimeter spatial resolution in the region in front of the polycarbonate, as seen in Fig. 2.

III. JET EVOLUTION AND GEOMETRY

False-color, logarithmic-scale photographs of the shot sequence recorded by the iCCD imaging system are presented in Figs. 3 and 4 for the $z_{\rm pc}=12$ cm and 17 cm cases, respectively. From these images, it is evident that there are three distinct stages in each shot sequence. Figures 3(a) and 4(a) depict the first stage, where the first jet travels unobstructed toward the polycarbonate sheet. Once the first jet collides with the polycarbonate [Figs. 3(b) and 4(b)], it becomes stagnated and starts to expand radially. While this expansion takes place, the second jet travels unobstructed toward the polycarbonate [Figs. 3(c) and 4(c)]. As the second jet collides with the expanding background plasma, it acts as a piston driving material back toward the polycarbonate. This results in the formation of a bright emission structure [Figs. 3(d) and 4(d)] which appears concurrently with a sharp increase in electron density measured by the interferometer.

Qualitative insights into jet geometry are also found in these images. For both obstruction cases, the jets display a distinct leading edge, with a width that is consistently larger than the thickness. The material driven by the piston action of the jet exhibits a curved leading edge, resembling a cohesive bow-shock structure that propagates through the background plasma. This curvature is also consistent with the interferometer traces (Sec. IV), which indicate that the density increase associated with collision is detected earlier in time along the bore-sight axis.

IV. AXIAL CHARACTERIZATION OF COLLISION EVENTS

The temporal evolution of phase shift measured by the interferometer chords is interpreted as line-integrated electron density in order to compare plasma density after the collision to the density of the jet and background. Measurements with chords at the same

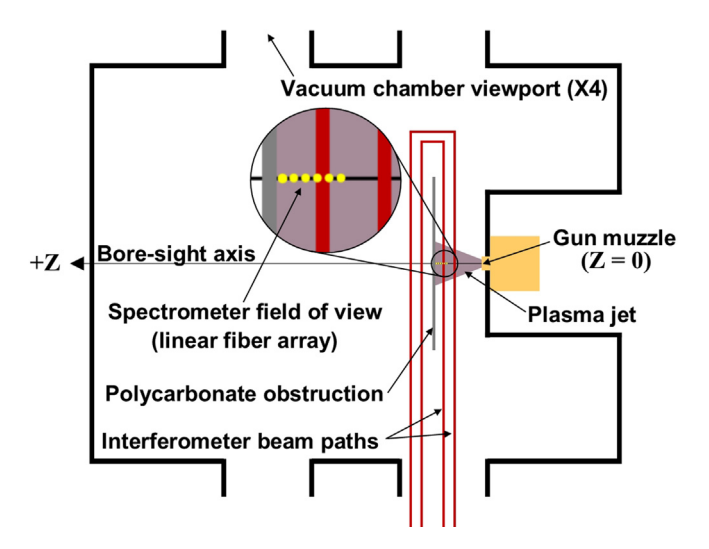


FIG. 2. Top–down cross sectional view of the vacuum chamber with the polycarbonate placed along the z-axis. ²² Interferometer chords pass through viewports located on the side of the chamber perpendicular to the bore-sight axis. Spectrometer optics are mounted on the top of the chamber to capture a top-down view of the plasma jets as they translate along the z-axis.

vertical position as the gun muzzle (y = 0 cm) and at two axial stations, $z_{\rm pc} - z = 1$ and $z_{\rm pc} - z = 2.5$ cm are presented in both Figs. 5 and 6.

The three distinct stages of the collision event are also evident in these density traces. First, each probe beam detects an initial local maximum in phase shift attributable to the unobstructed first jet passing each beam en route to the polycarbonate. Second, after the first jet passes both chords, there is a gradual rise in chord-integrated density $(n_e l)$ in the $z_{pc} - z = 1$ cm chord. This is interpreted to be the stagnated first jet slowly expanding back toward the gun muzzle after colliding with the polycarbonate. As the stagnated plasma is expanding, the second jet in the discharge cycle is detected at $z_{\rm pc}-z$ = 2.5 cm. This second jet exhibits less $n_e l$ than the first jet, which may be explained by depletion of neutral gas within the railgun; the ejection of the first jet leaves less mass to be accelerated as the second jet. Average time of flight measurements for the second jet measured at z = 9.5 and 14.5 cm suggests a jet velocity of 32.9 km/s. Shortly after the second jet passes the $z_{\rm pc}-z$ = 2.5 cm chord, a sharp peak is observed at $z_{\rm pc}-z$ = 1 cm. This peak has a significantly greater line-integrated density than the second jet. This enhancement in $n_e l$ corresponds to the bright emission structures observed in the iCCD images and is suggestive of compression or shock formation due to the collision between the second jet and stagnated first jet. The time domain for these collision events is referenced to t_0 which denotes the time at which this density feature passes the $z_{pc} - z = 1$ cm, y = 0 cm chord. Figure 5 describes the manner in which the line-integrated density traces are interpreted to identify the phases and features of the collision events.

V. RADIAL CHARACTERIZATION OF COLLISION EVENTS

Radial density profiles of the background and post-collision plasma have been studied by measuring line-integrated densities at varying heights above the bore-sight axis at $z_{\rm pc}-z=1$ cm. Because the interferometer is a two-chord system, these measurements required keeping one probe beam fixed at $z-z_{pc}=1$ cm, y=0 cm while independently varying the y-position of the second chord over multiple shots. Averaged interferometer traces from this study in Figs. 7 and 8 show that the line-integrated density decreases further from the center of the collision. Assuming an azimuthally symmetric density distribution, these measurements suggest that each jet has a non-uniform radial density profile with highest densities at the center. PiMAX images qualitatively corroborate these measurements, with the strongest plasma emission observed near the center and decreasing toward the edges of the jets. Features in density evolution attributable to interaction between the jet and stagnant plasma occur at successively later times in the off-axis chordal measurements, which is explained by the curved leading edge of the piston-compressed plasma observed in the iCCD images.

To compare the density of plasma immediately after the collision to the density of the stagnant plasma and that of the second jet, radial profiles of the unobstructed second jet are separately characterized at z=11 and z=14.5 cm. Presented in Figs. 9 and 10, these measurements also indicate a decrease in $n_e l$ with increasing y-position. At both z-locations, the second jet arrives at the y=0 and y=2 cm radial positions at approximately the same time, suggesting that the leading edge of the second jet is nearly planar in this region.

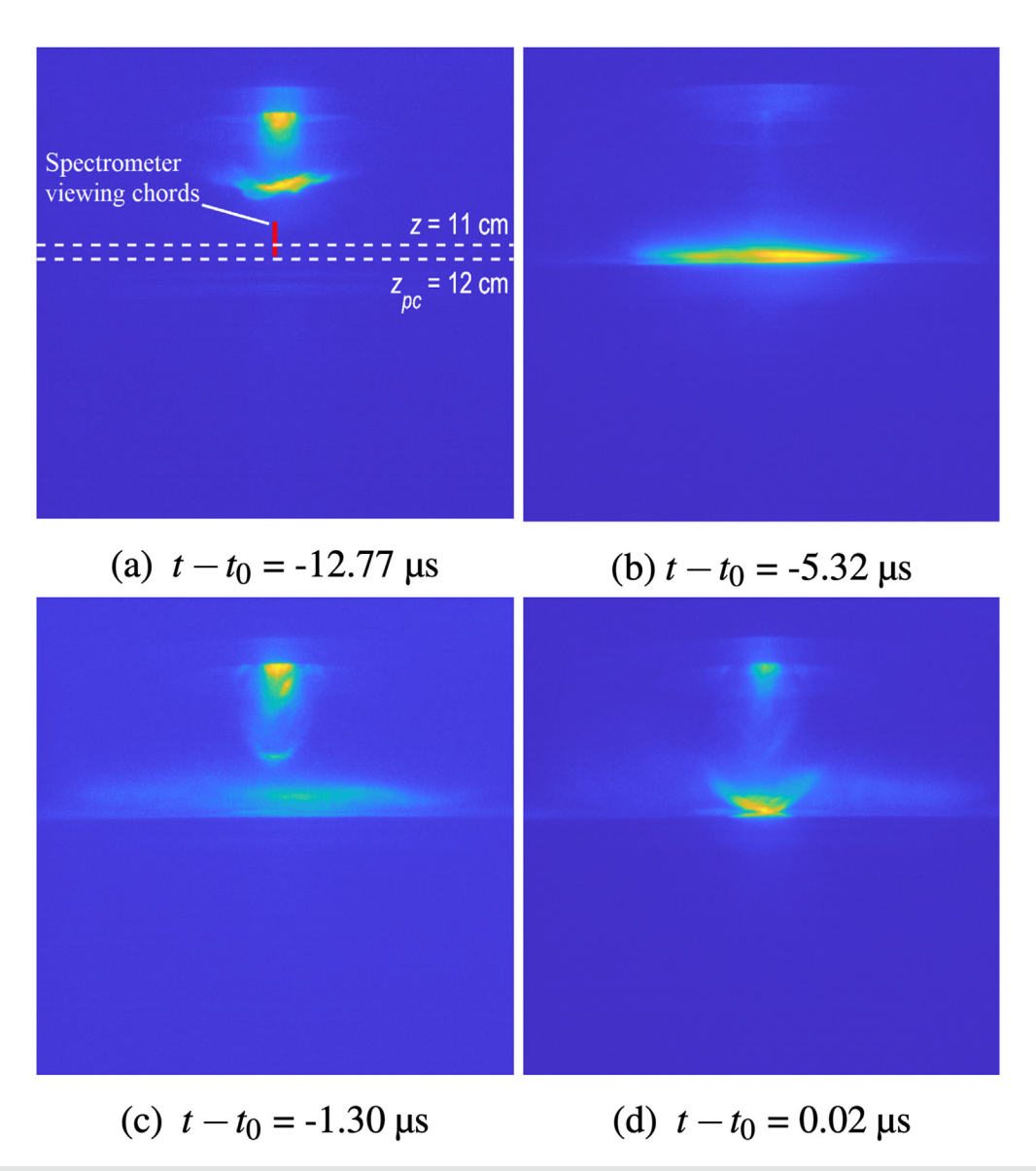


FIG. 3. False color, logarithmic-scale images of the collision event for the $z_{pc} = 12$ cm obstruction case; (a)–(d) are photographs of shots 1772, 1767, 1756, and 1754, respectively; a 3 ns exposure time was used for all images. Image time is presented relative to the time of flight of the post-collision plasma in the $z_{pc} - z = 1$, y = 0 cm chord.

For each obstruction location, transverse distributions of line-integrated density for different plasma features during the collision event are shown in Figs. 11 and 12. Note that all transverse profiles are reported for times where solely the identified feature is present at y=0 (see Fig. 5). Figures 11(b) and 12(b) depict this distribution using raw interferometer data. Due to the nature of the two chord interferometer setup, sample size varies with chord location, with only the y=0 cm chord being set up for all shots. To investigate the repeatability of density measurements over the dozens of shots presented here, the average line-integrated density at each off-axis chord position is normalized to the average on-axis $n_e l$ recorded for that shot set, resulting in radial

distribution models seen in Figs. 11(a) and 12(a). Multiplying the radial model for each subset of shots by the average on-axis $n_e l$ across all shots shows good agreement between the radial model and the averaged raw measurements, shown in Figs. 11(b) and 12(b). This agreement between the raw and modeled densities suggests that the average on-axis density did not significantly change across these experiments, an indication of the repeatability of experimental pulses. Assuming an axisymmetric plasma column, these density mappings may be used to infer jet width. The line-integrated density for the second jet at z=14.5 cm, for example, approaches zero at y=4 cm, suggesting that the jet width is roughly 8 cm at the z=14.5 station.

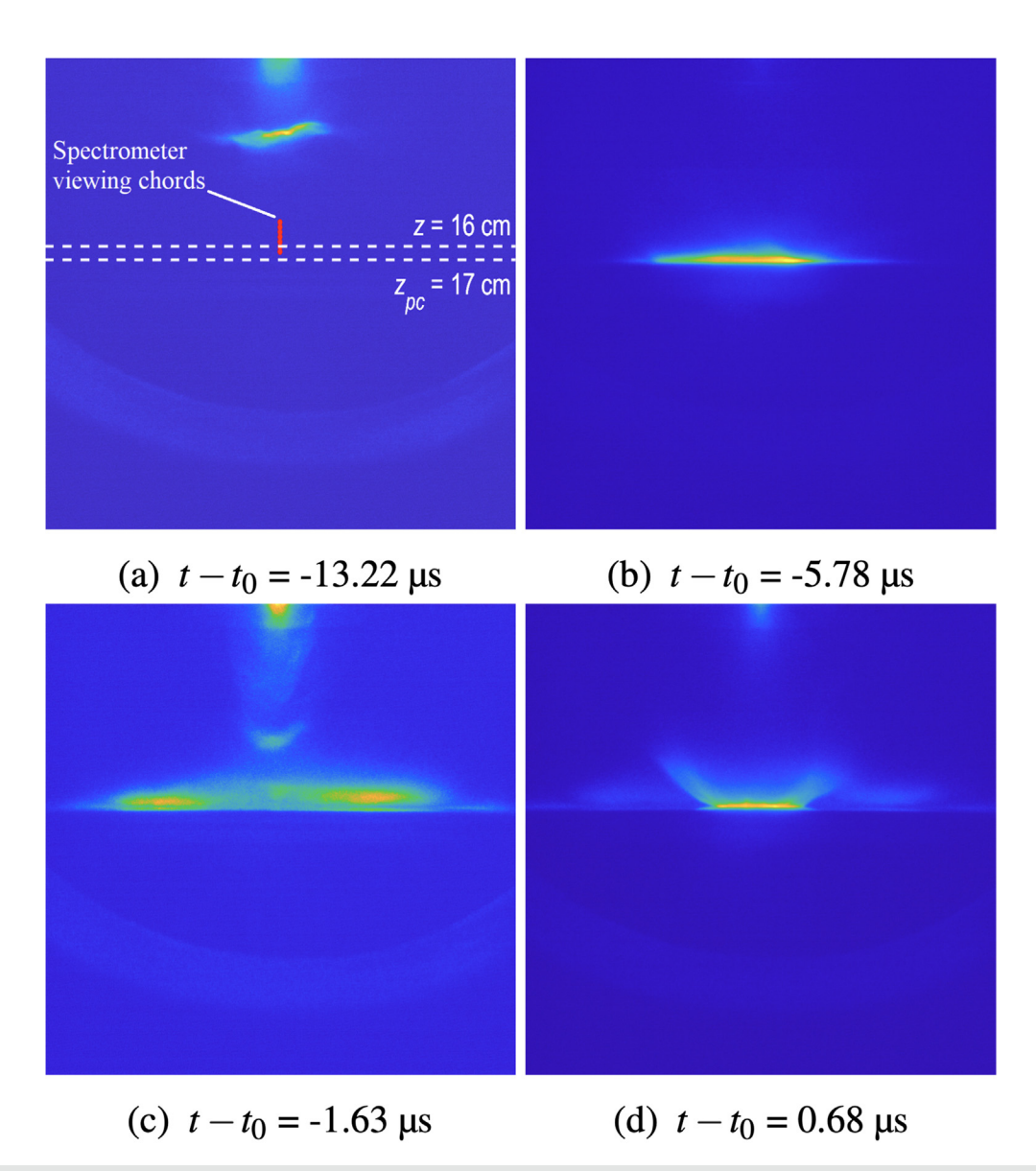


FIG. 4. False color, logarithmic-scale images of the collision event for the $z_{pc} = 17$ cm obstruction case; (a)–(d) are photographs of shots 1551, 1512, 1516, and 1536, respectively; a 3 ns exposure time was used for all images. Image time is presented relative to the time of flight of the post-collision plasma in the $z_{pc} - z = 1$, y = 0 cm chord.

VI. ELECTRON NUMBER DENSITY FROM INTERFEROMETER TRACES

The interferometer phase shift is proportional to electron density line-integrated along the chord length through the plasma.²³ For studies involving plasma shocks, gradients and non-uniformities may be present in the density profiles along each chord, highlighting the need to infer local values of electron density from chord-integrated measurements. Using the off-axis chordal measurements presented above, a matrix Abel inversion technique was utilized to infer the radial density distribution throughout the collision sequence.

The interferometer phase $\Delta \phi$ shift is proportional to the lineintegrated electron number density by^{1,23}

$$\Delta \phi = C \int n_e dl, \tag{1}$$

where $C = \frac{e^2 \lambda}{4\pi\epsilon_0 m_e c^2}$. The Abel transform assumes a shell model, depicted in Fig. 13, to deconvolve phase shift measurements taken at the same axial position but differing *y*-locations, resulting in electron densities, ²³

$$n_e(r) = \frac{1}{c\pi} \int_r^R \frac{d\Delta\phi}{dy} \frac{dy}{(y^2 - r^2)^{1/2}},$$
 (2)

where the plasma is assumed azimuthally symmetric with a circular cross section. Because we have interferometer measurements at

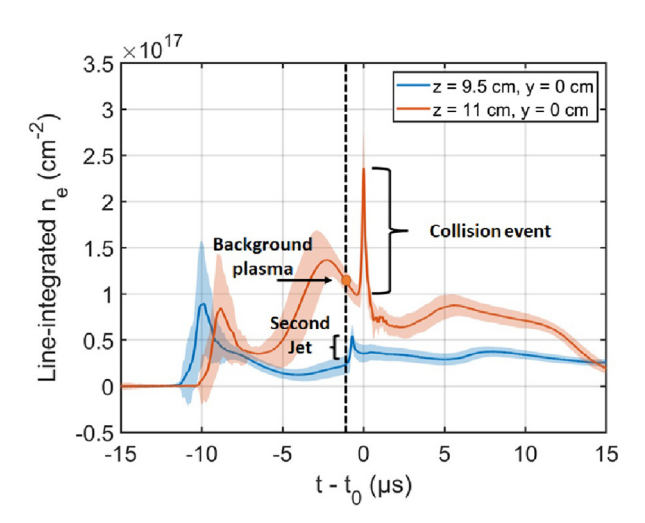


FIG. 5. Line-integrated electron density traces at two axial stations, inferred from phase shift measurements during collision events where the polycarbonate obstruction was placed at $z_{\rm pc}=12$ cm. Averages and 1σ standard deviation represent shots 1745 through 1812. Time is referenced relative to the time of peak density at z=11 cm, y=0 cm. Line-integrated densities associated with the precollision jets and post-collision plasma are taken to be the difference between the respective local maxima associated with each event and the line-integrated density recorded immediately preceding the event of interest. The density of the stagnated plasma at $z_{\rm pc}-z=1$ cm is measured at the moment before the arrival of the second jet at $z_{\rm pc}-z=2.5$ cm, which immediately precedes the collision event

discrete *y*-locations, the model is discretized into radial zones of constant density. 24 The number of radial zones corresponds to the number of chords probing the plasma. For interferometer chord *i*, the measured phase shift is given as

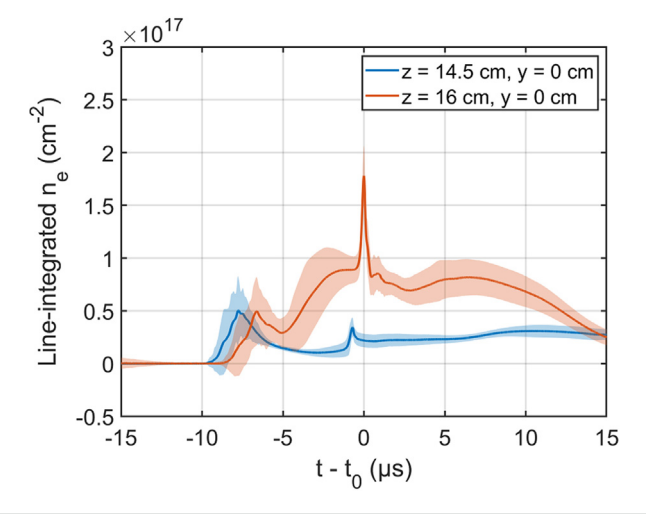


FIG. 6. Line-integrated electron density traces at two axial stations, inferred from phase shift measurements during collision events where the polycarbonate obstruction was placed at $z_{\rm pc}=17$ cm. Averages and 1σ standard deviation represent shots 1511 through 1586.

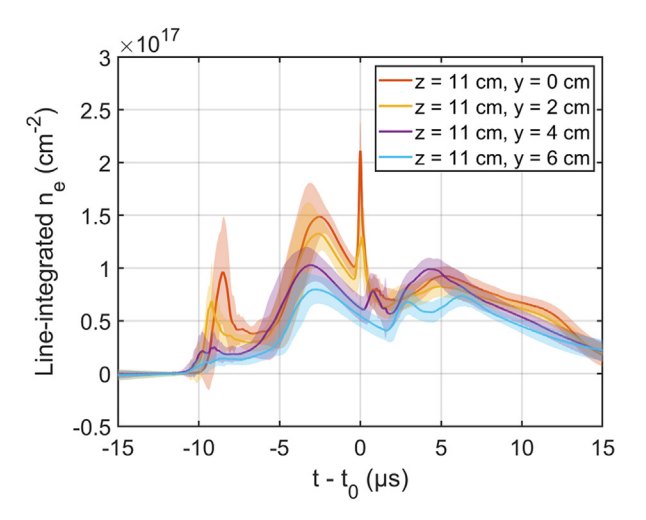


FIG. 7. Line-integrated electron density traces at four radial locations, inferred from phase shift measurements during collision events where the polycarbonate obstruction was placed at $z_{\rm pc}=12\,{\rm cm}$. Averages and 1σ standard deviation represent shots 1813 through 1885.

$$\Delta \phi_i = C \sum_j 2L_{i,j} n_{e_j},\tag{3}$$

which is analogous to the continuous, integral form presented above.²⁵ The length matrix L with elements $L_{i,j}$ specifies the path length for chord i through radial zone j in one quadrant of the plasma. The deconvolved density in the jth shell is then

$$n_{e_j} = \frac{1}{2C} \sum_{i} L_{j,i}^{-1} \Delta \phi_i.$$
 (4)

Based on the shell model in Fig. 13, geometry dictates that the length matrix \boldsymbol{L} is

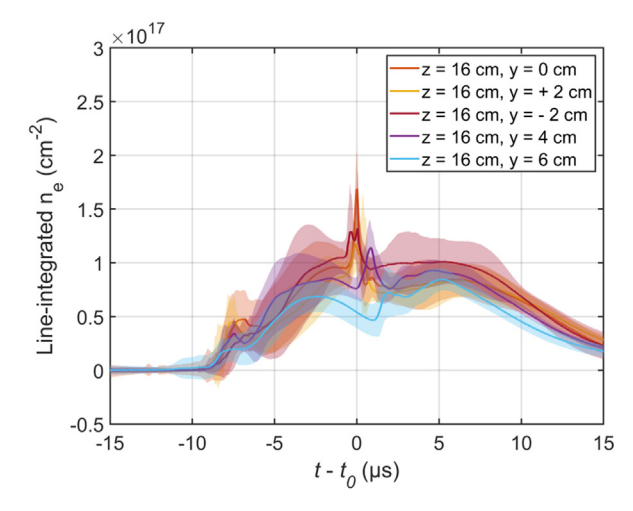


FIG. 8. Line-integrated electron density traces at five radial locations, inferred from phase shift measurements during collision events where the polycarbonate obstruction was placed at $z_{pc}=17\,\text{cm}$. Averages and 1σ standard deviation represent shots 1587 through 1712.

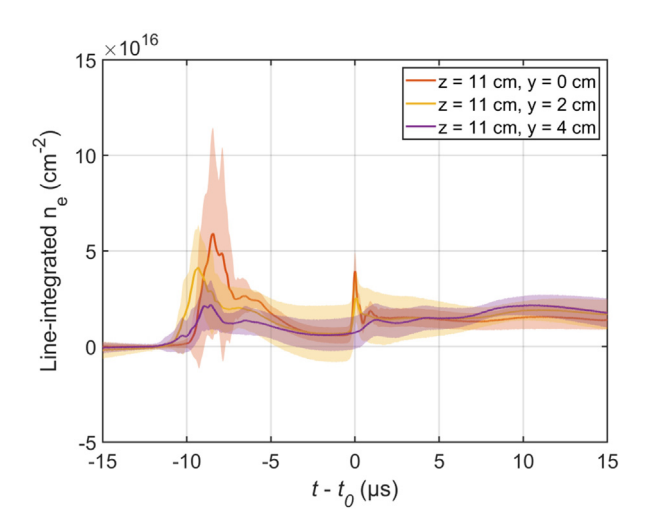


FIG. 9. Line-integrated electron density traces at three radial locations, inferred from phase shift measurements of the unobstructed second jet passing $z=11\,\mathrm{cm}$. Averages and 1σ standard deviation represent shots 1886 through 1923.

$$L_{i,i} = 0 (5)$$

for i > j,

$$L_{i,j} = \sqrt{y_{j+1}^2 - y_i^2} \tag{6}$$

for i = j, and

$$L_{i,j} = \sqrt{y_{j+1}^2 - y_i^2} - \sqrt{y_j^2 - y_i^2}$$
 (7)

for i < j. Using this inversion technique, the chord-integrated density distributions presented in Figs. 11(b) and 12(b) were used to infer electron density density for the three stages of the interaction (Figs. 14 and 15). The radially modeled data, which account for the varying

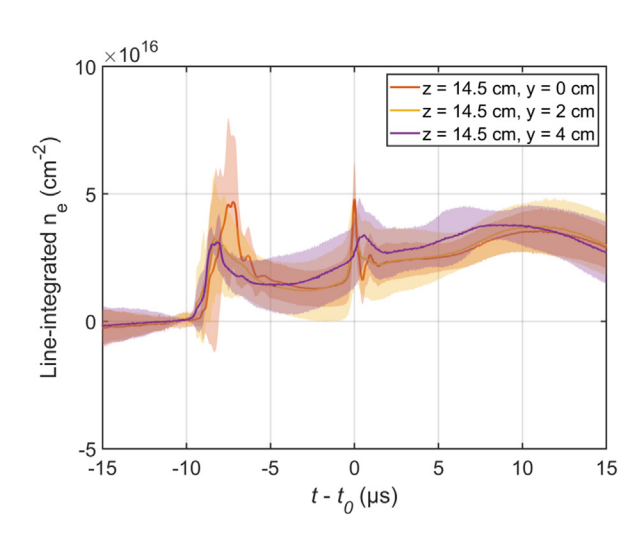
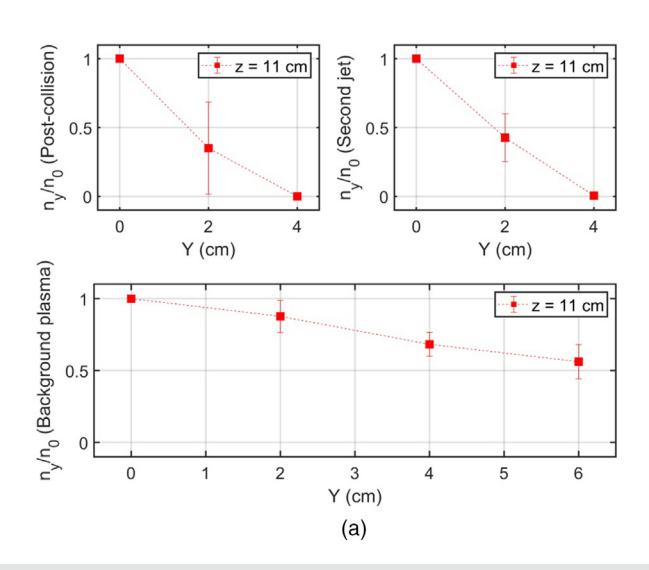


FIG. 10. Line-integrated electron density traces at three radial locations, inferred from phase shift measurements of the unobstructed second jet passing z=14.5 cm. Averages and 1σ standard deviation represent shots 1713 through 1739.

sample size in the experimental data sets, were used for this analysis. The unobstructed jet, stagnant background plasma, and "piston"-compressed plasma maintained the same trend of decreasing density with increasing radius. When the second jet is present at the axial station of the interferometer, the density drops dramatically by the $r=4\,\mathrm{cm}$ shell, suggesting a total jet width of $\approx 8\,\mathrm{cm}$. Conversely, chordal measurements for the background plasma at $y=6\,\mathrm{cm}$ are >50% that of their on-axis value, suggesting a total plasma width greater than 12 cm. To recover the radial distribution of the stagnant background electron density, we assume a boundary condition $n_e \rightarrow 0$ as $y \rightarrow 18\,\mathrm{cm}$. Although we do not suggest that the stagnant plasma possesses such a diameter at the time of arrival of the second jet, this



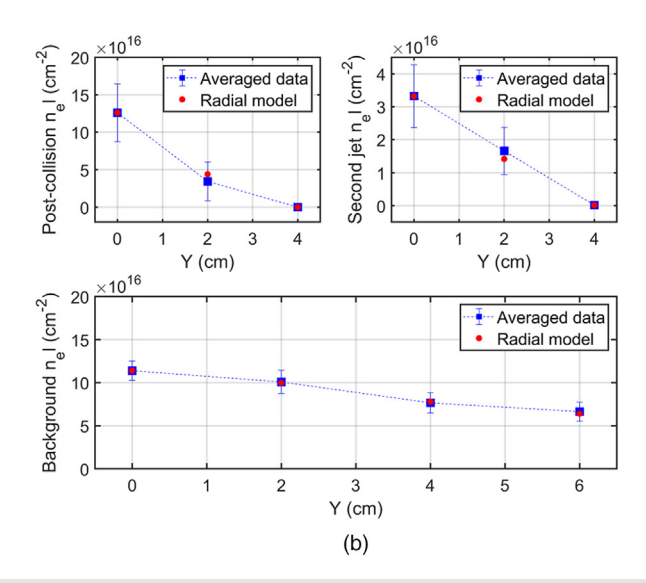
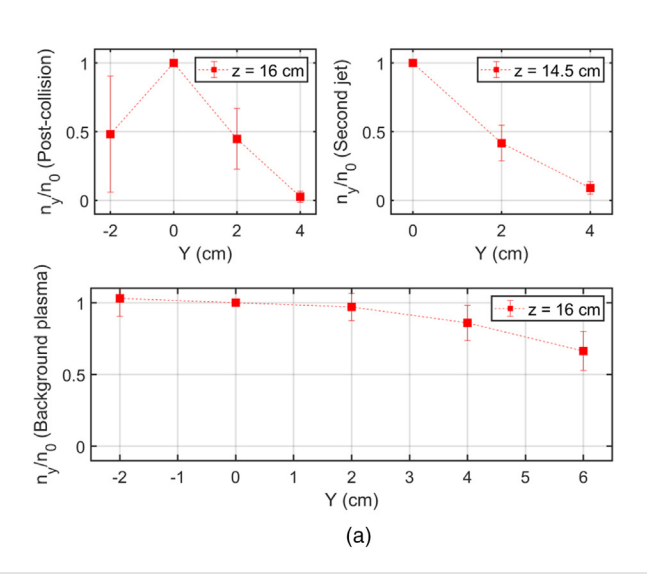


FIG. 11. Off-axis spatial distribution of line-integrated density of each component of the plasma for the $z_{pc} = 12$ cm obstruction case. Measurements for each component are reported at the time of arrival at the corresponding y = 0 cm, z = 11 cm interferometer chord (see Fig. 5).



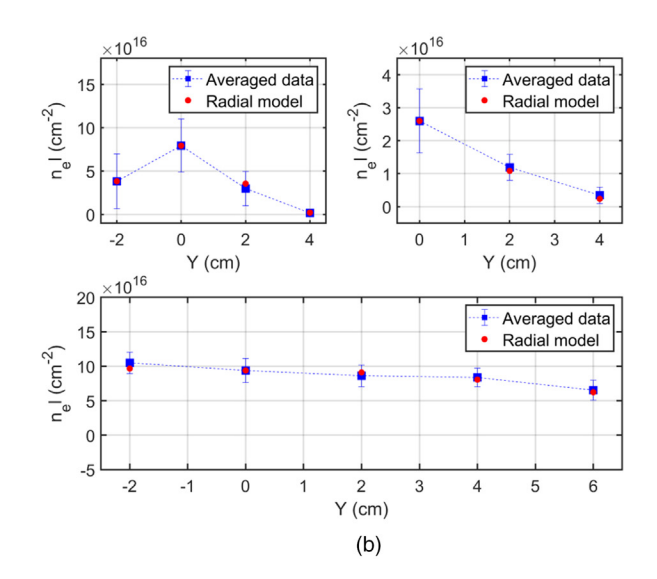


FIG. 12. Off-axis spatial distribution of line-integrated density of each component of the plasma for the $z_{pc} = 17$ cm obstruction case. Measurements for each component are reported at the time of arrival at the corresponding y = 0 cm interferometer chord.

would be physically enforced in the negative y-direction by an optical breadboard which supports the polycarbonate and lies 18 cm below the bore-sight axis. This boundary condition is treated as an additional sightline in the Abel inversion process. Additionally, chord-integrated densities presented in Fig. 12(b) show that $n_e l$ of the background plasma at the $y=\pm 2$ cm stations are approximately equal to the line-integrated density measured at y=0 cm. Therefore, the first shell in the background plasma model for the $z_{pc}=17$ cm case assumes a radius of 4 cm, with a density equal to the on-axis chord integrated measurement. Electron densities at r=0 are presented in Tables II and III, along with standard deviations which were propagated throughout the inversion process. The tabulated densities indicate that the collision produces a significant jump in density after the collision within a region of diameter 4 cm, despite the plasma being radially unconstrained.

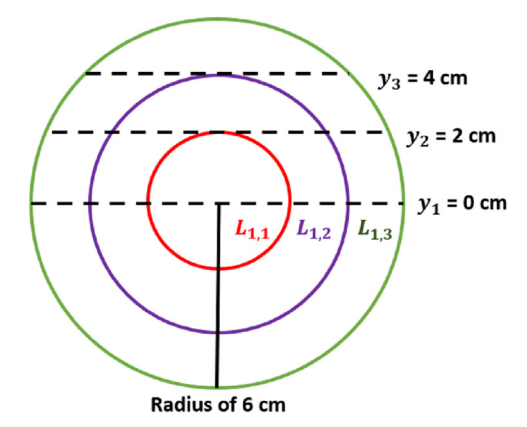


FIG. 13. Cross sectional view of plasma model used to infer densities through a matrix Abel inversion. Interferometer chords are assumed to be tangential to radial zones of constant density. The number of modeled radial zones corresponds to the number of sightlines used in experiment.

VII. INFERENCE OF IONIZATION FRACTION AND TEMPERATURE FROM PRISMSPECT SIMULATIONS

Estimates of T_e and \bar{Z} are used to evaluate the increase in ion density that occurs during collision events. Experimental spectrograms are compared to non-LTE simulations of spectra modeled using PrismSPECT. All simulations are steady-state, utilize a single-Maxwellian electron distribution, and assume an optically thin plasma. Capacitance manometer measurements of post-shot chamber pressure for gas-puff-only shots are 95 \pm 5% of the pressure measured after a full cycle of gas injection and energizing the railgun. The contributing impurities are assumed to consist of the accelerator's PEEK housing ($\rm C_{19}H_{12}O_3$) and ceramic insulators (70% AIN, 30% BN) by mass fraction. However, the carbon aluminum and boron impurities are not likely to contribute to the measured post-shot pressure. Assuming that

TABLE II. Electron densities and one sigma standard deviation inferred at r = 0 for the $z_{pc} = 12$ cm obstruction case.

	z (cm)	$n_e (\mathrm{cm}^{-3})$
Background	11	$8.3 \pm 2.1 \times 10^{15}$
Second jet	11	$6.3 \pm 2.0 \times 10^{15}$
Post-collision	11	$2.5 \pm 1.0 \times 10^{16}$

TABLE III. Electron densities and one sigma standard deviation inferred at r = 0 for the $z_{pc} = 17$ cm obstruction case.

	z (cm)	$n_e (\mathrm{cm}^{-3})$
Background	16	$4.4 \pm 1.2 \times 10^{15}$
Second jet	14.5	$4.8 \pm 1.9 \times 10^{15}$
Post-collision	16	$1.5 \pm 0.6 \times 10^{16}$

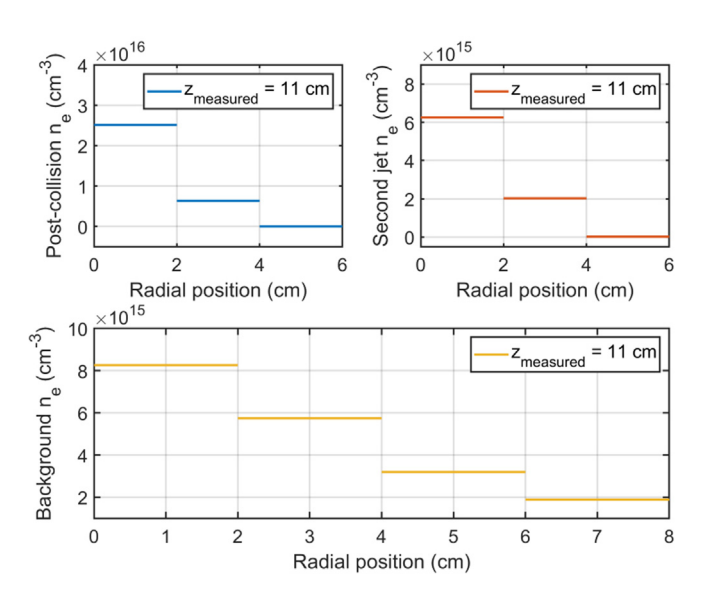


FIG. 14. Radial density distribution for all plasma components relevant to the z_{pc} = 12 cm obstruction case. Densities were inferred by applying the matrix Abel inversion to the radially modeled chordal density data in Fig. 11(b).

the mole fraction of impurity elements is equal parts PEEK and insulator, the stoichiometric makeup of these impurity components was used to interpret the capacitance manometer measurements, suggesting that plasma jet composition is $86 \pm 14\%$ argon. PrismSPECT simulations were run considering an argon composition of 86% (Table IV).

Experimental spectrograms capturing emission from a region colocated with the $y=0\,\mathrm{cm}$ interferometer chord (see Fig. 5) during different phases of the shot sequence were compared to PrismSPECT

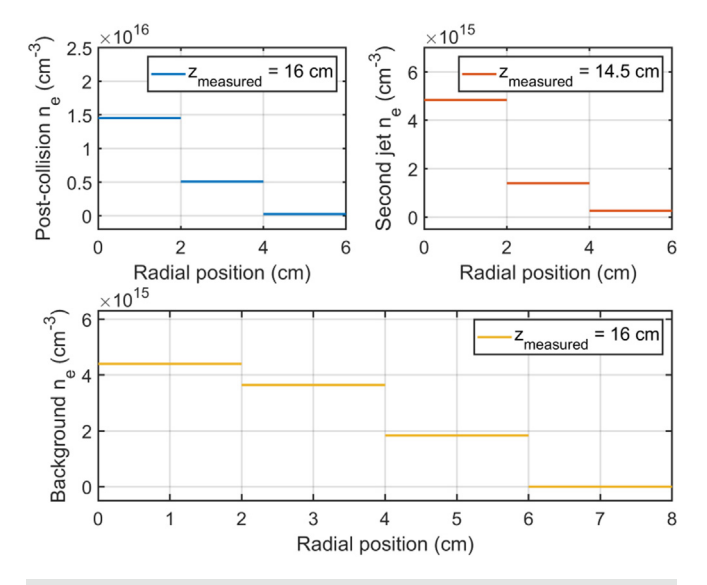


FIG. 15. Radial density distribution for all plasma components relevant to the z_{pc} = 17 cm obstruction case. Densities were inferred by applying the matrix Abel inversion to the re-constructed chordal density data in Fig. 12(b).

TABLE IV. Jet molar compositions used to model plasma emission in PrismSPECT.

Element	Molar percentage	
Ar	86.1 %	
С	3.9 %	
N	3.5 %	
Н	2.4 %	
В	1.4 %	
Al	2.0 %	
О	0.6 %	

modeling. For the compressed, post-collision plasma and pre-collision background plasma, this corresponded to the emission spectra recorded by the fiber aligned with the $z_{pc} - z = 1$ cm chord. Integration times of 200 ns were used to record these spectra. For characterization of the unobstructed second jet, spectrometer data recorded at fiber C4 was used to characterize the jet at z = 11 cm. Due to the weak emission intensity of the unobstructed jets, an exposure time of 3 μ s was required to improve the signal-to-noise ratio of associated spectrograms, which were solely used to infer the plasma parameters of the second jet. Representative spectra from different phases of the collision sequence are shown in Fig. 16. Over 90% of the lines in this survey belong to Ar-II, with higher ionization states, if present, expected to be observed at shorter wavelengths, around 350 nm. While the collision event does not produce an abundance of additional lines around 400 nm, line intensities and signal-to-noise ratios show that emission from the pre-collision plasma is noticeably dimmer. For each phase of the interaction and corresponding spectrogram, an iterative process was used to infer ionization state and temperature bounds. 3,4,27 By initially assuming that $n_i = n_e$, a simulated emission dataset is generated which allows for the estimation of T_e and \bar{Z} based on the presence and absence of simulated lines when compared to the experiment. This estimate of \bar{Z} allows for a better estimate of n_i , which is used as an input for the next set of simulations. The analysis is completed when the n_i estimated at the end of an iteration is within 10% of the n_i inferred from the previous iteration. The results of this analysis are presented in Tables V and VI.

In general, ionization fractions greater than unity are inferred during all phases of the shot sequence. It should be noted that the lower bound estimate of \bar{Z} for the second jet is less than that of the post-collision plasma. This suggests that the increased electron density after the collision event is in part due to the presence of multiply ionized species. However, this is likely not the main mechanism by which

TABLE V. Plasma parameters inferred from PrismSPECT for the 12 cm obstruction case. Jet composition specified as 86% argon, 14% impurities.

	z	T (eV)	$ar{Z}$	$n_i(\text{cm}^{-3})$
Background	11	T > 2.4	$\bar{Z} > 1.7$	$n_i > 5.0 \times 10^{15}$
Second jet	11	2.0-2.8	1.1-1.9	$3.3 \times 10^{15} 5.6 \times 10^{15}$
(pre-collision)				
Post-collision	11	2.4-2.6	1.7-1.8	1.4×10^{16} – 1.5×10^{16}

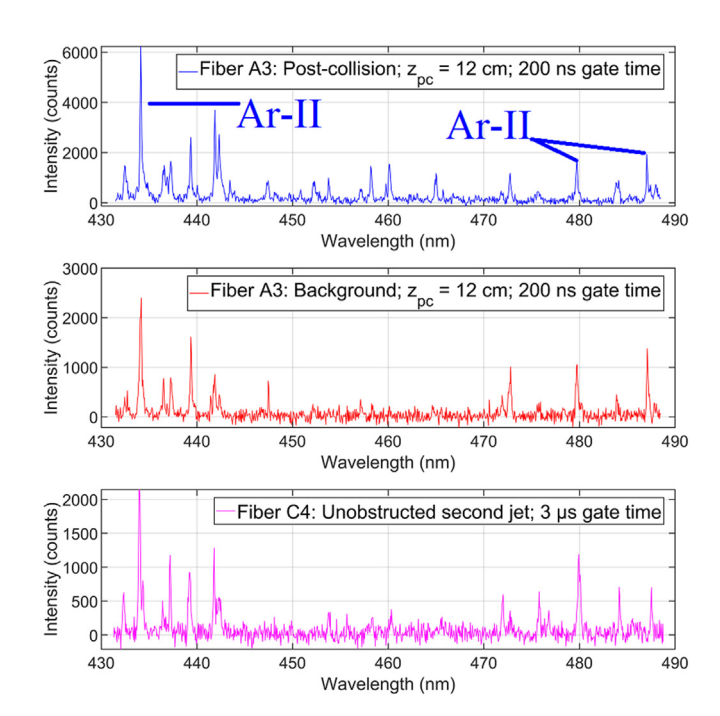


FIG. 16. Representative emission spectra corresponding to the three key phases of the collision sequence. These spectrograms were compared to PrismSPECT simulations to infer plasma parameters for the $z_{pc} = 12$ cm obstruction case.

electron density increases, given that the inferred ionization fractions during all phases of the interaction are less than 2. Rather, it is believed that the piston-like action of the second jet compresses the stagnant plasma, increasing ion density, and consequently electron density.

Based on the temperature and mean charge state inferred for the second jet, the Mach number,

$$M = \frac{u_0}{\sqrt{\gamma \bar{Z}} \frac{k_B T_e}{\bar{m}_i}},\tag{8}$$

is estimated in the range 6.8–10.4 ($\gamma=5/3$). These unobstructed, high Mach number jets have been previously shown to expand adiabatically in vacuum. Thus, their temperature and ionization fraction are assumed to be changing slowly relative to jet transit timescales upon arrival at the polycarbonate. The PrismSPECT parameters inferred for the second jet at z=11 cm were used to infer the ion density of the jet at z=14.5 cm. A semi-analytic model assuming adiabatic expansion was

 $\begin{tabular}{ll} \textbf{TABLE VI.} Plasma parameters inferred from PrismSPECT for the 17 cm obstruction case. Jet composition specified as 86% argon, 14% impurities. \end{tabular}$

	z	T (eV)	$ar{Z}$	$n_i(\text{cm}^{-3})$
Background		2.4-2.8		
Second jet	16	2.0-2.8	1.1-1.9	$2.2 \times 10^{15} - 3.8 \times 10^{15}$
(pre-collision)				
Post-collision	16	2.4-2.6	1.7-1.8	$7.9 \times 10^{15} - 8.8 \times 10^{15}$

then used to estimate the second jet density at z=16, r=0 cm. This model estimates the jet diameter at z=14.5 cm to be ≈ 8 cm (Fig. 15), which was inferred from on-axis interferometer data. Assuming a cylindrical plasma column aligned with the bore-sight axis, changes to the plasma volume as it traveled from z=14.5 to 16 cm were estimated assuming that the jet expands radially and axially at the ion thermal speed. This extrapolated density is then compared to the post-collision density at z=16, r=0 cm to characterize the change in density that occurs by inducing collision with the stagnant plasma rather than passing unobstructed through the chamber. Interferometer measurements of the unobstructed second jet at z=11 cm are compared with the post-collision densities at this location for the $z_{\rm pc}=12$ cm experiments to conduct a similar analysis of density enhancement.

To assess whether the density enhancement due to jet merging is indicative of a shock, the quantity $\chi = n_{\text{merged}}/(n_{\text{single}} + n_{\text{background}})$ is computed using the ion density estimates resulting from PrismSPECT modeling. The results of this analysis are reported in Table VII. In the event that interpenetration occurs upon jet merging, the density enhancement would not exceed a value of unity.2 This threshold is exceeded for both obstruction locations, suggesting that rather than simply passing through the background plasma, the second jet rapidly decelerates and compresses as it collides with the stagnated first jet, forming a shock. Since the ion density of the second jet and background plasma are nearly equal, the experimental post-collision-tosecond-jet density jump is $\approx 2\chi$. For $\gamma = 5/3$, the Rankine–Hugoniot conditions predict a theoretical post-collision-to-second-jet density jump between 3.8 and 3.9. While this roughly agrees with the empirical upper bound estimates for χ , the lower bounds of the experimental data (i.e., a density jump of \approx 2.4) are highly plausible and could be explained by radial pressure relief and plasma equation of state effects, causing deviation from the 1D analytical prediction.

VIII. INFERENCE OF GRADIENTS IN DENSITY FROM OBSERVATION OF STARK BROADENING IN EXPERIMENTAL SPECTROGRAMS

Axial density distributions are inferred from Stark broadening of the Ar-II line at 488 nm, which is recorded with the spatially resolved spectroscopy diagnostic. While line emission recorded by the spectrometer is chord-integrated, we interpret the envelope of the recorded profile to correspond to the greatest broadening along the viewing chord and consequently the greatest density. Experimental line profiles are assumed to take the shape of a Voigt profile, which can be deconvolved into a Gaussian component which accounts for Doppler broadening and a Lorentzian profile which accounts for Stark broadening.²⁸ The instrument profile of the spectrometer was also observed to be a Voigt profile. As a result, Stark and Doppler widths were deconvolved from instrument effects by treating the effective Lorentzian and Gaussian widths as

TABLE VII. Ion density enhancement, χ , due to jet collision for both obstruction locations. Jet composition specified as 86% argon, 14% impurities.

$\overline{z_{ m pc}({ m cm})}$	12	17
z_{measured} (cm) $n_{\text{collision}}/(n_{\text{background}} + n_{\text{jet2}})$	11 1.3–1.8	16 1.2–2.0

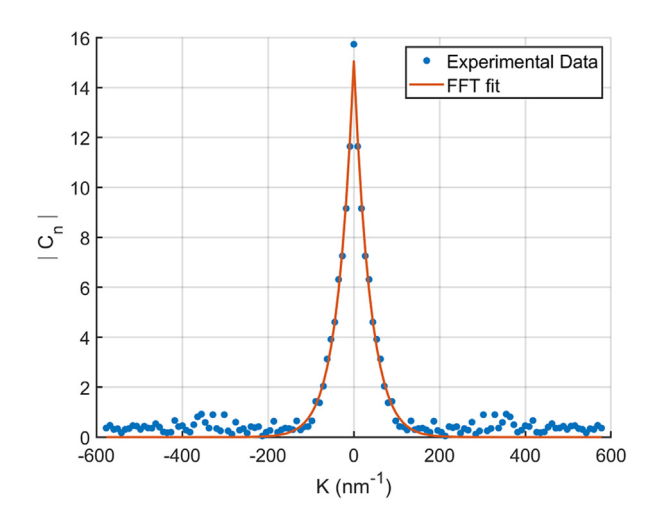


FIG. 17. Measurement of electron density via Stark broadening of the Ar-II line at 488 nm for the post-collision plasma in the $z_{\rm pc}=12\,{\rm cm}$ obstruction case (shot 1800 fibers A1–A2). A Voigt profile is fitted to the magnitude of the discrete Fourier transform of the experimental data. ²⁸

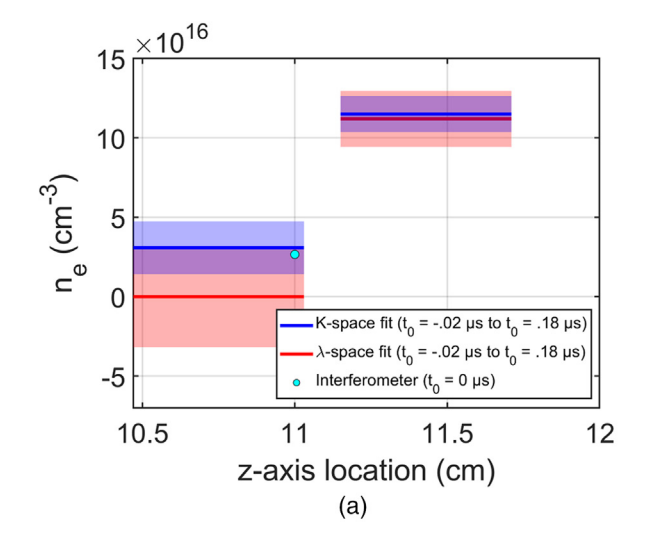
$$L_w = L_{Stark} + L_{Instrument} \tag{9}$$

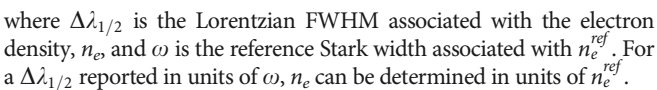
and

$$G_w = \sqrt{G_{Doppler}^2 + G_{Instrument}^2}, \tag{10}$$

respectively. For non-hydrogenic ions, such as argon, Stark broadening is primarily due to electron impact effects and scales linearly with density according to the relation²⁹

$$\Delta \lambda_{1/2} = \omega \frac{n_e}{n_e^{ref}},\tag{11}$$





Given an experimental line profile, the Lorentzian and Gaussian FWHM is inferred by fitting a Voigt profile to the magnitude of the discrete Fourier transform of the experimental data. These Fourier fits of Stark-broadened spectra have been shown to be less susceptible to noise and neighboring lines. This procedure is initially performed on lines measured using a HgAr spectral calibration lamp to determine the instrument function. A Fourier fit is then applied to the experimental data to obtain plasma parameters. Finally, the plasma parameters inferred from the Fourier fit were compared to parameters inferred from a wavelength space line fit.

This analysis was performed on experimental data recorded at a time the post-collision bow structure was present among the spectroscopy viewing chords. For the $z_{\rm pc}=12$ cm case, this consisted of the four fibers closest to the polycarbonate. For the $z_{\rm pc}=17$ cm case, this consisted of the two fibers closest to the polycarbonate. To improve the signal to noise ratio in the emission data, experimental intensity was summed across pairs of fibers. For the $z_{\rm pc}=12$ cm case, these represented the total intensity measured in fibers A1–A2 and A3–A4, respectively. For the $z_{\rm pc}=17$ cm case, this represented the total emission in fibers B1–B2. Figure 17 details the Fourier fitting process for the line emission measured in fibers A1–A2 of shot 1800. For all shots used for Stark broadening analysis, the spectrometer was equipped with a 2400 g/mm diffraction grating, resulting in wavelength dispersion of 0.0054 nm per pixel. An exposure time of 200 ns was used for these shots.

Axial density distributions captured at the time of peak interferometer phase shift in the $z_{\rm pc}-z=1$ cm chord during the collision between the second jet and stagnant plasma are presented in Fig. 18 for both obstruction locations. Standard deviation in the fitted parameters, interpreted as $\approx 1/2$ of the 95% confidence interval for each parameter was propagated alongside the standard deviation in the

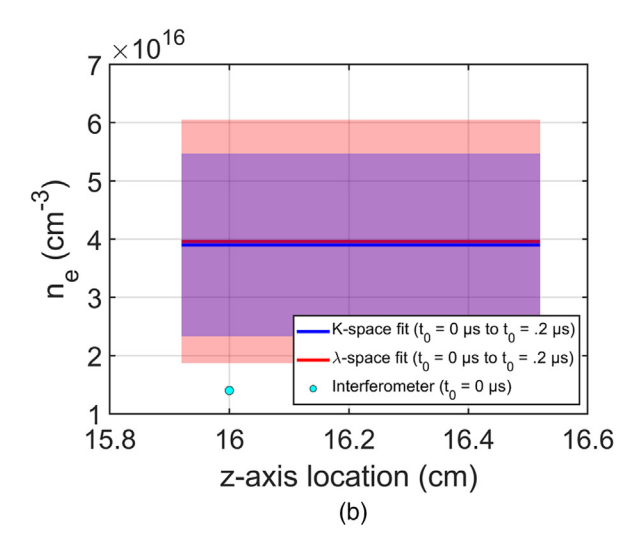


FIG. 18. Axial electron density distribution for the post-collision plasma inferred from line-broadening and interferometer measurements. Gel shaded regions represent estimated 1-sigma standard deviation in electron density. The Abel-inverted interferometer measurements from $z - z_{pc} = 1$ cm correspond to the peak plasma density measured during the 200 ns spectrometer gate time.

TABLE VIII. Comparison of theoretical ion penetration lengths assuming jet composition of 86% argon.

<i>z</i> _{pc} (cm)	12	17
$\lambda_{i,Ar}^{s}$ (mm)	2.1-5.9	3.3-11
$\lambda_{i,Ar}^{s}$ (mm) $\lambda_{i,C}^{s}$ (mm)	0.3-0.9	0.6-1.7

instrument profile measurements to estimate the uncertainty in the plasma parameters. For the 17 cm case, the density inferred at $z_{\rm pc}-z=1\,{\rm cm}$ is higher than the densities predicted from the chordintegrated interferometer measurements at the same location. This is likely due to the localized nature of the spectrometer measurements, which allow for density to be estimated in millimeter-sized regions rather than averaged over shells several centimeters in diameter. The k-space and λ -space fits show good agreement, with the exception of fits to the emission spectra from fibers A3 and A4 (10.47 $\leq z \leq$ 11.03 cm) for the 12 cm case. In this instance, the wavelength fit predicts significantly lower electron density than the Fourier fit. This discrepancy can in part be explained by the appreciably lower signal-to-noise ratio of the corresponding emission profile and resulting high fit residual in comparison to the other attempted fits. While the k-space fit also has a high fitting residual, it infers a density close to the Abel-inverted interferometer measurement from the same location. For the $z_{pc} = 12 \text{ cm}$ case, there is a significant increase in density that occurs closer to the polycarbonate, with an inferred electron density an order of magnitude greater than the densities at z = 11 cm. This axial density gradient is consistent with the formation of a collisional shock and suggests additional compression and density enhancement beyond the extent of the interferometer chord located at the $z_{pc} - z = 1$ cm station.

IX. ESTIMATION OF COLLISIONALITY PARAMETERS AND THEIR RELEVANCE TO SPECIES SEPARATION IN PLASMA SHOCKS

Collision parameters have been estimated for both obstruction locations to assess jet collisionality. Table VIII displays estimations of ion–ion penetration lengths, which represent the distance that an ion from the unobstructed second jet will stream through the stagnated background plasma (denoted by a prime) without making frequent collisions.² The ion penetration length is given as 1,2,30

$$\lambda_i^s \approx \frac{u_{rel}}{4\nu_s^{|i|'}},\tag{12}$$

where $\nu_s^{i|l'}$ is the collision rate given in the limit of fast ions 1,30 computed using the Coulomb logarithm for counterstreaming ions. 1,30

The test particles considered for these computations were Ar-II and C-II. In addition to both generating prominent spectral lines in the experimental spectrograms, there is a significant variation in atomic weight between these two particles. The field particle mass was approximated as the weighted average of the constituent elements in plasma, with the molar percentages in Table IV serving as the corresponding weights. Second jet and stagnant plasma parameters in Tables V and VI were used as the test and field particle plasma parameters.

Table IX displays estimations of ion-ion mean-free-path for the shock-compressed plasma. This is given as

TABLE IX. Comparison of ion-ion mean-free-path in shock-compressed plasmas, assuming jet composition of 86% argon.

$z_{\rm pc}$ (cm)	12	17
$\lambda_{i,\mathrm{Ar}}$ (μ m) $\lambda_{i,\mathrm{C}}$ (μ m)	7-8 6-7	11-13 10-11

$$\lambda_i \approx \frac{u_i}{\nu_{\varepsilon}^{|i|'}},\tag{13}$$

where u_i corresponds to the velocity of a test ion (un-primed) in the post-collision plasma, and $\nu_i^{|i|'}$ is the energy loss rate calculated using the full formulation for Coulomb-collision rates and the Coulomb logarithm for mixed ion–ion collisions. These calculations model a test particle from the downstream plasma as it travels with velocity u_i and kinetic energy $\varepsilon = m_i u_i^2/2$ and interacts with an isotropic Maxwellian distribution of field ions. The test ion velocity u_i is set to the thermal speed. Based on analysis of line broadening, we assume that $T_{i'} \approx T_i \approx T_e$ for these calculations. The field particle ion density, $n_{i'}$ corresponds to the post-shock ion density inferred from PrismSPECT, while the test particle ion density is calculated as $n_i = (\% \text{ abundance}) \times n_{i'}$, where the percent abundance of the ion species is inferred from Table IV. Once again test particles of Ar-II and C-II were used for these calculations.

Stark broadening measurements presented in Fig. 18 suggest that the gradient scale length of the shock compressed plasma is $\approx\!1$ cm. All tabulated ion–ion penetration lengths and mean free paths are less than or on the order of this characteristic length, which suggests that the interaction between the second jet and background plasma is semi- to fully collisional. The difference between argon and carbon penetration lengths suggest that the heavier species penetrates farther into the stagnant plasma before becoming collisional, which could give rise to species separation due to kinetic effects in the vicinity of the shock.

We now turn to fluid theory to quantitatively characterize the various diffusion mechanisms at play at the shock front. Diffusion theory suggests that in the center-of-mass frame of a binary species mix, the mass diffusive flux of the lighter species is equal and opposite to that of the heavier species, ^{5,8,17} such that

$$\overline{f_l} = \rho_l \nu_{Dl} = -\overline{f_h} = -\rho_h \nu_{Dh}, \tag{14}$$

where ρ_b ρ_h and ν_{Db} , ν_{Dh} are the light and heavy ion species mass densities and center-of-mass diffusion velocities, respectively.

The diffusive mass flux for the lighter ion species in the center-of-mass frame is expressed as

TABLE X. Comparison of diffusion parameters for both obstruction cases. $f_{\rm 1Baro}$ and $f_{\rm 1Electro}$ correspond to the second and fifth terms in parenthesis in Eq. (15).

$z_{\rm pc}$ (cm)	12	17
k_{Pi}/k_E	0.62-0.64	0.62-0.64
$\overline{f_{1_{\mathrm{Baro}}}}/\overline{f_{1_{\mathrm{Electro}}}}$	3.1-4.6	2.7-4.0
$\nabla \log(P_i)/\nabla \log(T_i)$	4.4-6.5	3.8-5.6

$$\overline{f_l} = -\rho D \left(\nabla c_{ml} + k_p \nabla \log(P_l) + k_{Ti} \nabla \log(T_i) + k_{Te} \nabla \log(T_e) + \frac{e k_e \nabla \Phi}{T_i} \right),$$
(15)

where ρ is the light-plus-heavy ion mass density, and pre- to post-shock gradients in total ion pressure, average ion temperature (where we assume $T_{il} \approx T_{ih} \approx T_e$), electron temperature, and electrostatic potential give rise to baro-diffusion, thermo-diffusion, and electro-diffusion. While the baro-diffusion k_{pi} and electro-diffusion coefficients k_E can be evaluated analytically, the electron and ion thermo-diffusion coefficients, as well as the diffusion coefficient, D, require a kinetic treatment to obtain a tractable solution. 5,8,17

Table X presents the estimation of parameters relevant to the mass flux of the light ion species in the post-shock plasma. We approximate our plasma as consisting of a heavy ion species (argon) and a light ion species, whose mass is the weighted average of the impurity elements in the plasma. The ratio of the baro- to electro-diffusion coefficients shows that electro-diffusion works to reinforce baro-diffusion. By estimating the gradient in plasma potential as $\nabla T_e/e$, we present the ratios of baro-diffusion and electron-diffusion mass flux terms [second and fifth terms in parenthesis in Eq. (15)], which suggests that baro-diffusion dominates over electro-diffusion. While the thermo-diffusion coefficients require a more detailed analytical treatment, the ratio of the experimental pressure jump to ion temperature jump suggests that baro-diffusion is likely the dominant mechanism by which gradient-driven species separation could be induced in this experiment.

X. SUMMARY

The campaign reported in this paper characterizes the collision between a supersonic jet with stagnated plasma, both produced using a small linear railgun. Jet stagnation was achieved using a polycarbonate sheet to obstruct the propagation of an initially supersonic jet through a cylindrical vacuum chamber. Collisions were induced between the stagnant plasma and a second high Mach number jet at distances of $z_{pc} = 12$ and 17 cm from the muzzle of the gun. In both obstruction cases, high speed photography, interferometry, and spatially resolved spectroscopy captured the formation of a high density layer during the collision. Plasma parameters inferred from non-LTE spectral modeling suggest that for both obstruction cases, the enhancement in ion density during the collision event significantly exceeds the threshold for kinetic interpenetration. Ion-ion penetration lengths and mean free paths estimated for both obstruction locations further suggest semi- to fully collisional behavior of ion species. Axial density distributions of the post-collision plasma inferred from Stark broadening display a density gradient across the thickness of the plasma, consistent with the formation of a collisional shock. Comparison of experimental results to diffusion theory suggests that baro-diffusion is the dominating diffusion mechanism at the shock front.

ACKNOWLEDGMENTS

The authors are grateful for the technical support and efforts of many student researchers over the years, specifically that of Maximilian Schneider. This work was supported by the National Science Foundation under Grant No. PHY-1903442.

AUTHOR DECLARATIONS Conflict of Interest

The authors have no conflicts to disclose.

Author Contributions

A. I. Mohammed: Data curation (lead); Formal analysis (lead); Investigation (equal); Methodology (supporting); Visualization (lead); Writing – original draft (lead); Writing – review and editing (supporting). C. S. Adams: Conceptualization (lead); Data curation (supporting); Formal analysis (supporting); Funding acquisition (lead); Investigation (equal); Methodology (lead); Project administration (lead); Resources (lead); Supervision (lead); Visualization (supporting); Writing – original draft (supporting); Writing – review and editing (lead).

DATA AVAILABILITY

The data that support the findings of this study are available from the corresponding author upon reasonable request.

REFERENCES

- ¹M. K. Schneider, A. I. Mohammed, and C. S. Adams, "Characterization of plasma jets driven by a small linear railgun," Plasma Sources Sci. Technol. 29, 045013 (2020).
- ²E. C. Merritt, A. L. Moser, S. C. Hsu, C. S. Adams, J. P. Dunn, A. Miguel Holgado, and M. A. Gilmore, "Experimental evidence for collisional shock formation via two obliquely merging supersonic plasma jets," Phys. Plasmas 21, 055703 (2014).
- ³A. L. Moser and S. C. Hsu, "Experimental characterization of a transition from collisionless to collisional interaction between head-on-merging supersonic plasma jets," Phys. Plasmas 22, 055707 (2015).
- ⁴C. S. Adams, A. L. Moser, and S. C. Hsu, "Observation of Rayleigh-Taylor-instability evolution in a plasma with magnetic and viscous effects," Phys. Rev. E 92, 051101 (2015).
- ⁵G. Kagan and X.-Z. Tang, "Electro-diffusion in a plasma with two ion species," Phys. Plasmas **19**, 082709 (2012).
- ⁶C. Bellei, H. Rinderknecht, A. Zylstra, M. Rosenberg, H. Sio, C. Li, R. Petrasso, S. Wilks, and P. Amendt, "Species separation and kinetic effects in collisional plasma shocks," Phys. Plasmas 21, 056310 (2014).
- plasma shocks," Phys. Plasmas 21, 056310 (2014).

 B. D. Keenan, A. N. Simakov, W. T. Taitano, and L. Chacón, "Ion species stratification within strong shocks in two-ion plasmas," Phys. Plasmas 25, 032103 (2018)
- ⁸T. Byvank, S. J. Langendorf, C. Thoma, and S. C. Hsu, "Observation of shockfront separation in multi-ion-species collisional plasma shocks," Phys. Plasmas 27, 042302 (2020).
- ⁹H. G. Rinderknecht, H.-S. Park, J. Ross, P. Amendt, S. Wilks, J. Katz, N. Hoffman, G. Kagan, E. Vold, B. Keenan *et al.*, "Measurements of ion velocity separation and ionization in multi-species plasma shocks," Phys. Plasmas 25, 056312 (2018)
- ¹⁰S. C. Hsu, T. R. Joshi, P. Hakel, E. L. Vold, M. J. Schmitt, N. M. Hoffman, R. M. Rauenzahn, G. Kagan, X.-Z. Tang, R. C. Mancini *et al.*, "Observation of interspecies ion separation in inertial-confinement-fusion implosions," Europhys. Lett. 115, 65001 (2016).
- ¹¹T. R. Joshi, P. Hakel, S. C. Hsu, E. L. Vold, M. J. Schmitt, N. M. Hoffman, R. M. Rauenzahn, G. Kagan, X.-Z. Tang, R. Mancini et al., "Observation and modeling of interspecies ion separation in inertial confinement fusion implosions via imaging x-ray spectroscopy," Phys. Plasmas 24, 056305 (2017).
- 12 T. R. Joshi, S. C. Hsu, P. Hakel, N. M. Hoffman, H. Sio, and R. Mancini, "Progress on observations of interspecies ion separation in inertial-confinement-fusion implosions via imaging x-ray spectroscopy," Phys. Plasmas 26, 062702 (2019).
- ¹³P. Amendt, O. Landen, H. Robey, C. Li, and R. Petrasso, "Plasma barodiffusion in inertial-confinement-fusion implosions: Application to observed yield

- anomalies in thermonuclear fuel mixtures," Phys. Rev. Lett. 105, 115005 (2010).
- ¹⁴P. Amendt, S. Wilks, C. Bellei, C. Li, and R. Petrasso, "The potential role of electric fields and plasma barodiffusion on the inertial confinement fusion database," Phys. Plasmas 18, 056308 (2011).
- ¹⁵O. Larroche, "Ion Fokker-Planck simulation of D-3He gas target implosions," Phys. Plasmas 19, 122706 (2012).
- ¹⁶C. Bellei, P. Amendt, S. Wilks, M. Haines, D. Casey, C. Li, R. Petrasso, and D. Welch, "Species separation in inertial confinement fusion fuels," Phys. Plasmas 20, 012701 (2013).
- ¹⁷G. Kagan and X.-Z. Tang, "Thermo-diffusion in inertially confined plasmas," Phys. Lett. A 378, 1531–1535 (2014).
- ¹⁸E. Vold, R. Rauenzahn, and A. Simakov, "Multi-species plasma transport in 1D direct-drive ICF simulations," Phys. Plasmas 26, 032706 (2019).
- ¹⁹J. C. Wheeler, R. P. Harkness, Z. Barkat, and D. Swartz, "Supernovae, supernebulae, and nucleosynthesis," Publ. Astron. Soc. Pac. 98, 1018 (1986).
- ²⁰D. A. Swartz, J. C. Wheeler, and R. P. Harkness, "Model light curves of linear type II supernovae," Astrophys. J. 374, 266–280 (1991).
- ²¹F. Bufano, S. Immler, M. Turatto, W. Landsman, P. Brown, S. Benetti, E. Cappellaro, S. Holland, P. Mazzali, P. Milne *et al.*, "Ultraviolet spectroscopy of supernovae: The first two years of swift observations," Astrophys. J. **700**, 1456 (2009).

- ²²M. K. Schneider, "Characterization of collisional shock structures induced by the stagnation of railgun-driven multi-ion-species plasma-jets," Ph.D. thesis (Virginia Tech, 2020).
- 23. H. Hutchinson, Principles of Plasma Diagnostics, 2nd ed. (Cambridge University Press, 2002).
- ²⁴I. B. Gornushkin, S. V. Shabanov, and U. Panne, "Abel inversion applied to a transient laser induced plasma: Implications from plasma modeling," J. Anal. At. Spectrom. 26, 1457–1465 (2011).
- ²⁵R. E. Bell, "An inversion technique to obtain full poloidal velocity profiles in a tokamak plasma," Rev. Sci. Instrum. 68, 1273–1280 (1997).
- ²⁶See www.prism-cs.com for "Prism Computational Sciences."
- ²⁷S. Hsu, E. Merritt, A. Moser, T. Awe, S. Brockington, J. Davis, C. Adams, A. Case, J. Cassibry, J. Dunn *et al.*, "Experimental characterization of railgun-driven supersonic plasma jets motivated by high energy density physics applications," Phys. Plasmas 19, 123514 (2012).
- ²⁸G. Vogman and U. Shumlak, "Deconvolution of stark broadened spectra for multi-point density measurements in a flow Z-pinch," Rev. Sci. Instrum. 82, 103504 (2011).
- ²⁹M. Burger and J. Hermann, "Stark broadening measurements in plasmas produced by laser ablation of hydrogen containing compounds," Spectrochim. Acta Part B 122, 118–126 (2016).
- ³⁰J. Huba, NRL Plasma Formulary Supported by the Office of Naval Research (Naval Research Laboratory, Washington, DC, 2013).